water

MDPI

Article

Dynamic Response Law and Failure Mechanism of Slope with Weak Interlayer under Combined Action of Reservoir Water and Seismic Force

Wenpeng Ning [1,2] and Hua Tang [2,*]

[1] School of Civil Engineering, Architecture and Environment, Hubei University of Technology, Wuhan 430068, China; ningwenpeng1998@163.com
[2] State Key Laboratory of Geomechanics and Geotechnical Engineering, Institute of Rock and Soil Mechanics, Chinese Academy of Sciences, Wuhan 430071, China
* Correspondence: hua005066@163.com

Abstract: The southwestern region of China is close to the Eurasian earthquake zone. Many engineering areas in southwestern China are affected by earthquakes and are close to the epicenter of earthquakes that occur in this region. During earthquakes, slopes with weak interlayers are more likely to cause large-scale landslides. In response to the low stability of slopes with weak interlayers in reservoir dam areas, the dynamic response law and failure mechanism of weak interlayered slopes under the combined action of reservoir water and seismic forces were studied through shaking table model tests and finite element numerical simulation software. The height of the water level and the size of the seismic waves were changed during these tests. The research results indicate that seismic waves are influenced by weak interlayers and are repeatedly superimposed between the weak interlayers and the slope surface, resulting in an acceleration amplification effect that increases by approximately 1.8 times compared to homogeneous slopes. Vertical earthquakes have a significant impact on the dynamic response of slopes, and their peak acceleration amplification coefficient can reach 0.83 times the horizontal peak acceleration. The stability of weak interlayers during earthquakes is the worst within the range of the direct action of reservoir water. The failure mode of a slope is as follows: earthquake action causes cracking in the upper part of the slope, and as the earthquake increases in intensity, and the infiltration of reservoir water intensifies, the cracks expand. The soft and muddy interlayer in the front section of the slope forms a sliding surface, and ultimately, the sliding failure forms an accumulation body at the foot of the slope. In reservoir dam areas, the stability of a slope is closely related to the engineering safety of the reservoir dam. Therefore, when a strong earthquake and the water level in a reservoir jointly affect a weak-interlayer slope, the slope is in the stage of plastic deformation and instability. The stability of the slope may be overestimated, and the slope is likely vulnerable to sliding instability, which needs to be monitored and treated.

Keywords: weak intercalation; vibration table test; dynamic response; permanent displacement; reservoir water slope; argillization

Citation: Ning, W.; Tang, H. Dynamic Response Law and Failure Mechanism of Slope with Weak Interlayer under Combined Action of Reservoir Water and Seismic Force. *Water* **2023**, *15*, 1956. https://doi.org/10.3390/w15101956

Academic Editors: Stefano Morelli, Veronica Pazzi and Mirko Francioni

Received: 7 April 2023
Revised: 18 May 2023
Accepted: 19 May 2023
Published: 21 May 2023

1. Introduction

In southwest China, the Earth's crust moves vigorously, with strong earthquakes frequently occurring. Large crustal uplift in this area has formed hills, deeply embedded rivers, and high and steep slopes. In the vast mountainous area in this region, a large amount of side (sliding) slopes are distributed. Vast engineering construction projects are taking place in the southwest to cut paths in mountains and meet water to build bridges, resulting in a large number of artificial slopes. Reservoir areas contain weak mezzanine slopes, which occupy a considerable proportion of these areas. As a kind of weak structural layer, the elastic modulus and strength of soft interlayers are lower than that of surrounding rock. Under the combined action of reservoir water and a strong earthquake, rocks are more

likely to slip along the soft interlayer, resulting in major geological disasters and serious economic and livelihood losses [1,2]. For example, the 7.3-magnitude earthquake in Taiwan in 1999 caused a large number of bedding landslides (partial weak interlayer landslides), resulting in multiple traffic interruptions, and the maximum area affected by the landslides reached 5 square kilometers [3]. In 2008, the Tangjiashan landslide in Beichuan swept into a river valley, blocked the Jianjiang River channel, formed the dammed Tangjiashan lake, killed 84 people, and threatened the lives of 1.3 million who lived downstream of the river [4]. The landslide of Zhengjiashan in Pingwu buried houses, schools, and roads at the foot of the slope, causing a large number of casualties, including students and villagers, and direct economic losses of about CNY 3.5 million [5]. Therefore, it is very important to study the stability of slopes under the combined effect of water and an earthquake in an earthquake-stricken area; it is especially important to determine the damage process and sliding instability mechanism of weak sandwiches under the influence of water and an earthquake.

Physical model tests [6–9] and numerical simulation tests [10–12] are important methods of studying the stability of different factors. Domestic and foreign scholars have carried out much research on the stability of a slope under the effect of water, mainly focusing on changes in a slope's stability and the forms of its destruction alongside changes in the water level. Wang, R., Jiang, Z.H., and others used physical models to imitate the fluctuation of the water level in a river, which proved that changes in the water level would seriously endanger the stability of a slide. Among these changes, the distortion and destruction of the slide mostly occurred in the weak sandwiched area, and the model construction showed similar results [13,14]. Upomo, T.C. et al. analyzed a landslip caused by a change in the water level due to heavy rain through a numerical simulation. Then, a model was established to predict the damage caused by the landslip [15]. Many research results have been obtained on the dynamic response of slopes under the effect of an earthquake [16]. K. L. Wan and M. L. Lin carried out research based on the limit balance analysis, PIV analysis, and accelerated time history records. They used the vibration table model to study the starting and destruction process of a slope [17]. Hailong Yang and others studied the dynamic response of a saturated weak sandwiched slope under the effect of multiple earthquakes. They demonstrated that the response increased with the increase in the input wave, but they did not carry out a qualitative analysis [18]. Wang Liwei used the Newmark sliding block analysis method to study whether the dynamic safety factor and permanent displacement of a slope under vertical seismic action were considered [19]. Yan Zhixin et al. used the finite difference method to compare the similarities and differences in a slope's dynamic response with or without a vertical earthquake [20].

Many studies have been carried out on the stability of rock slopes under the combined effect of water and earthquakes, but few of them have focused on the two major factors: water and an earthquake. Most of them have focused on the dynamic response of a dam under the combined effect of water and an earthquake, and the mechanism of weak sandwiches in a slope has scarcely been studied. Under the combined effect of water and the force of an earthquake, the dynamic response of a slope with weak sandwiches was studied. The indoor vibration platform model test and the limited element simulation software were used to study the dynamic response mechanism of a slope with weak sandwiches under the combined effect of water and the force of an earthquake and to analyze the impact of soft sandwiches on the transmission of earthquake waves. It was clear that weak sandwiches were destroyed under the influence of water and the force of an earthquake and the sliding and losing mechanism.

Section 2 illustrates and briefly explains the preparation work for the preliminary model test: determining the parameters, similarity ratio, material ratio, monitoring point layout, and loading seismic plan. Section 3 discusses the dynamic response and displacement law for each monitoring point on the slope surface based on an analysis of the simulation results of the vibration table. Section 4 describes work in which numerical simulation software was used to calculate and analyze the dynamic response and perma-

nent displacement law of the slope, which was compared and verified with the model test results. Section 5 summarizes the triggering factors and failure mechanisms in the sliding of weak intercalated slopes under the action of reservoir water and seismic forces, based on observations of the failure morphology of the slope. The conclusions are presented in Section 6.

2. Shaking Table Model Test Scheme

2.1. General Situation of Engineering Geological Environment

The water depth in front of the dam in the reservoir area of the hydropower station is about 130 m. This section of the valley is a V-shaped, longitudinal monoclinic valley with symmetrical topography on both sides. The mountain is abundant and the terrain is rugged, and the slope topography is largely uniform, as shown in Figure 1. Due to the influence of the tropospheric occurrence and the steep slope along the river, the two sides of the bank slope form a stepped topography. The left bank is a downhill slope with an overall slope of 20°–30°. A series of 30 m–60 m high and continuous steep ridges develop diagonally along the bank slope, and the slopes of steep ridges can reach more than 45°.

Figure 1. Topography of engineering area.

The outcrop beds in the engineering area are mainly the upper part of the upper Permian basalt formation, including basalt, almond basalt, volcanic breccia lava, and tuff, as shown in Figure 2. According to 13 boreholes and 3 adits at the dam site, the tuff is produced in layers with a thickness of 1 m–2 m, and there is obvious extrusion, dislocation, and argillation between the tuff and the tuff layer. Due to changes in the water level, the front section of the tuff interlayer is immersed for a long time in reservoir water, which leads to the gradual formation of slime in the soft interlayer with good permeability, and the corresponding strength parameters are greatly reduced, which seriously affects the stability of the reservoir slope.

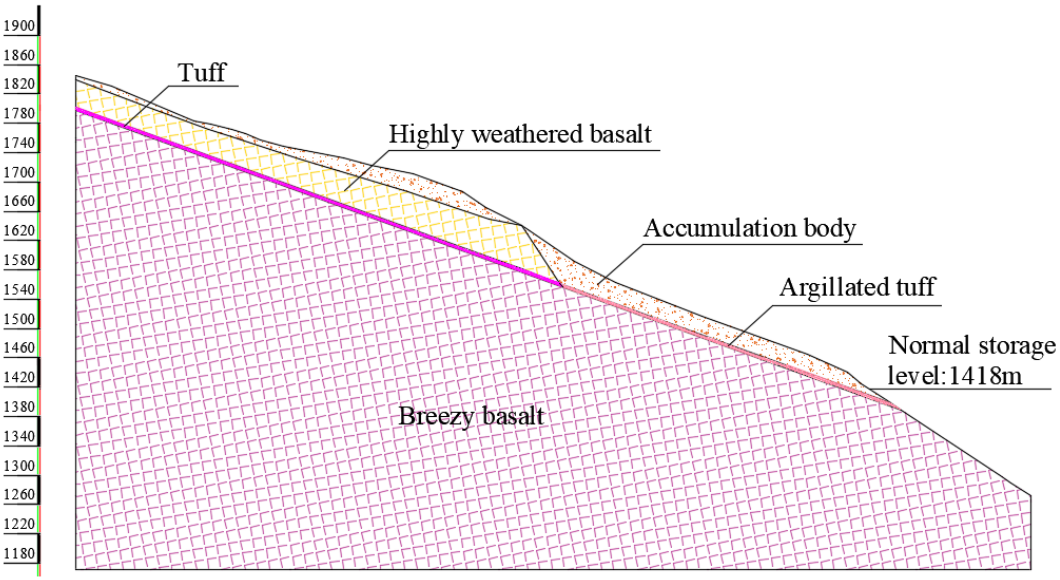

Figure 2. Geological section of the left bank of the reservoir area.

2.2. Determining the Physical Parameters of Each Rock Layer

According to the borehole and adit sampling test near the engineering area, the shear strength, tensile strength, and compressive strength of basalt were measured using a triaxial test. See Figure 3 for the instrument used in the test and the test curve. The specifications of the main machine of the MTS815−03 triaxial testing machine were as follows: static, 2667 kN; tensile load, 1335 kN; and loading rigidity of cross member, 10.5×10^9 N/m. The maximum lateral pressure of the triaxial pressure chamber of the test machine was 500 MPa. Specimen size was $\Phi 50 \sim 100$ mm $\times$ $(100 \sim 150)$ mm; measuring range of displacement was ± 50 mm; range of strain measurement was ± 0.03 mm. Four pieces of equipment are commonly used for in situ shear tests: pressure plate (size 500×500 mm); loading system−hydraulic jack; reaction system−transmission column with sufficient stiffness and 360×360 mm bracket; measuring system−a pressure gauge, dial gauge, and magnetic gauge holder.

(**a**) (**b**)

Figure 3. Laboratory and in situ tests. (**a**) Model MTS815−03 Triaxle Tester. (**b**) Original rock shear test.

For the calculation and analysis, we determined the physical and mechanical parameters of the rock mass with weak interlayers in the reservoir area, as shown in Table 1, by comprehensively considering indoor tests and field tests such as the deformation of rock mass and the shear resistance of rock mass and weak surfaces and consulting recommended values from various codes and empirical values from hydraulic manuals. It can be seen from the table that the mechanical parameters of the argillized layer of tuff are lower than those of tuff.

Table 1. Physical and mechanical parameters of rock mass.

Material Name	Volume Weight γ/kN/m^3	Elasticity Modulus E/MPa	Poisson's Ratio μ	Cohesion c/Mpa	Frictional Angle $\varphi/^\circ$
Accumulation body	24	25	0.38	0.03	31
Highly weathered basalt	30	1000	0.26	0.8	35
Tuff	29	80	0.30	0.09	28
Argillated tuff	30	40	0.33	0.05	24
Breezy basalt	30	20,000	0.23	1.5	43

Based on their theoretical and practical experience in rock behavior, H ° ek and Br ° wm established the principal stress relationship for rock mass failure, namely the H ° ek−Br ° wm criterion. By linking this criterion with *RMR*, the strength parameters of the rock mass can be estimated. The H ° ek−Br ° wm criterion has the following relationship:

$$\sigma_1 = \sigma_3 + \sqrt{m\sigma_c\sigma_3 + s\sigma_3} \quad (1)$$

In the formula, σ_1 is the maximum stress at failure; σ_3 is the minimum principal stress acting on the rock mass; m and s are the rock material constant.

The key to applying the above equation is how to determine the material parameters, the m and s values, of rocks. H ° ek and Br ° wm introduced the *RMR* classification system into the criteria and proposed using the following equation to estimate the material constants m and s:

For disturbed rock masses:

$$\frac{m}{mi} = \exp\left(\frac{RMR - 100}{14}\right) \quad (2)$$

$$s = \exp\left(\frac{RMR - 100}{6}\right) \quad (3)$$

For undisturbed rock mass:

$$\frac{m}{mi} = \exp\left(\frac{RMR - 100}{28}\right) \quad (4)$$

$$s = \exp\left(\frac{RMR - 100}{9}\right) \quad (5)$$

In the formula, m and s are the material parameters of the rock mass; mi is the m value of a complete rock.

Once the m and s values have been calculated, the normal stress on the sliding surface of the slope can be estimated, and C is determined according to the tangent line of the

envelope of the main stress circle in the definition of the H ° ek−Br ° wm criterion, φ. The specific process is as follows:

$$\begin{cases} h = 1 + 16(m\sigma_n + s\sigma_c)/3m^2\sigma_c \\ \theta = [90^\circ + \arctan(1/\sqrt{h^3 - 1})]/3 \\ \phi = \arctan(1/\sqrt{4h\cos^2\theta - 1}) \\ \tau = (\cot\phi - \cos\sigma)m\sigma_c/8 \\ C = \tau - \sigma_n \tan\phi \end{cases} \tag{6}$$

2.3. Similar Relationships and Material Ratios

Being affected by the site, quantity, and economy, an indoor model test usually reduces the model size according to similar criteria. In order to achieve change characteristics that are as close as possible to the actual engineering and create a similar relationship between the slope model and bridge site slope prototype, the compatibility equation, physical equation, geometric equation, balance equation, and boundary condition of the slope model and bridge site slope prototype should be guaranteed. The similar relationship is shown in the following formula, where m represents the physical quantity of the slope model, and p represents the physical quantity of the slope prototype at the site:

$$C_\sigma = C_1 = C_x, \qquad C_\sigma = C_\varepsilon C_E, \qquad C_\mu = 1, \qquad C_\varepsilon = 1, \qquad C_x = C_\sigma \tag{7}$$

C_σ is the stress ratio:

$$C_\sigma = \frac{(\sigma_x)_p}{(\sigma_x)_m} = \frac{(\sigma_y)_p}{(\sigma_y)_m} = \frac{(\tau_{xy})_p}{(\tau_{xy})_m} = \frac{\sigma_p}{\sigma_m} \tag{8}$$

C_l is the geometric proportion:

$$C_l = \frac{x_p}{x_m} = \frac{y_p}{y_m} = \frac{u_p}{u_m} = \frac{v_p}{v_m} = \frac{l_p}{l_m} \tag{9}$$

C_ε is the strain ratio:

$$C_\varepsilon = \frac{(\varepsilon_x)_p}{(\varepsilon_x)_m} = \frac{(\varepsilon_y)_p}{(\varepsilon_y)_m} = \frac{(\varepsilon_{xy})_p}{(\varepsilon_{xy})_m} = \frac{\varepsilon_p}{\varepsilon_m} \tag{10}$$

C_E is the modulus of elasticity ratio:

$$C_E = \frac{E_p}{E_m} \tag{11}$$

C_μ is Poisson's ratio:

$$C_\mu = \frac{\mu_p}{\mu_m} \tag{12}$$

The above equation is satisfied, and the similar relationship between the slope model and the prototype of the bridge site slope is consistent. According to the similarity theory [21,22], the similarity constant of the basic dimension of this test is determined from the actual size of the slope with weak interlayers and the inside diameter of the model box: the dimension similarity constant $C_l = 400$; the density similarity constant $C_\rho = 1$; the vibration acceleration similarity constant $C_a = 1$. We determined the size of the experimental model to be 2.6 m × 1.4 m × 1.5 m (length × height × width). As shown in Table 2, according to the dimension analysis method [23,24] and the Buckingham quantitative method [25], the similar constants of other physical quantities were calculated. Based on

the main similarity ratios of the model tests and repeated matching tests, the material ratios corresponding to the physical and mechanical parameters of each rock layer in the model were determined (see Table 3).

Table 2. Main similarities between model tests.

Physical Quantity	Similar Relationships	Similarity Ratio
Geometric dimension L	C_L	400
Accelerated speed a	$C_a = 1$	1
Material density ρ	C_ρ	1
Cohesion c	$C_c = C_\rho \times C_L$	400
Friction angle φ	$C_\varphi = 1$	1
Unit weight γ	$C_\gamma = C_\rho$	1
Elastic modulus E	$C_E = C_\rho \times C_L$	400
Poisson's ratio μ	$C_\mu = 1$	1

Table 3. Material ratio and parameters for model test.

Material Name	Material Ratio	Cohesion *c*/kPa	Friction Angle *φ*/°
Accumulator	Talc powder: Sand 2.4:1.6	1.55	31.8
Strongly weathered basalt	Steel slag: Sand: Gypsum: Water 5:4:1.3:2.2	9.3	34.4
Microweathered basalt	Iron powder: Barite powder: Water: Cement 30.0:10.0:3.5:1.4	14.3	43.4
Tuff	Hardboard	0.9	26.6

2.4. Layout of Monitoring Points

According to the layout principle of monitoring points and considering the influence of a tuff interlayer on the dynamic response of a slope with a weak interlayer, 15 monitoring points were set on the slope surface, interlayer, overburden, and bedrock (see Figure 4) to monitor the acceleration time history change process of a slope during an earthquake.

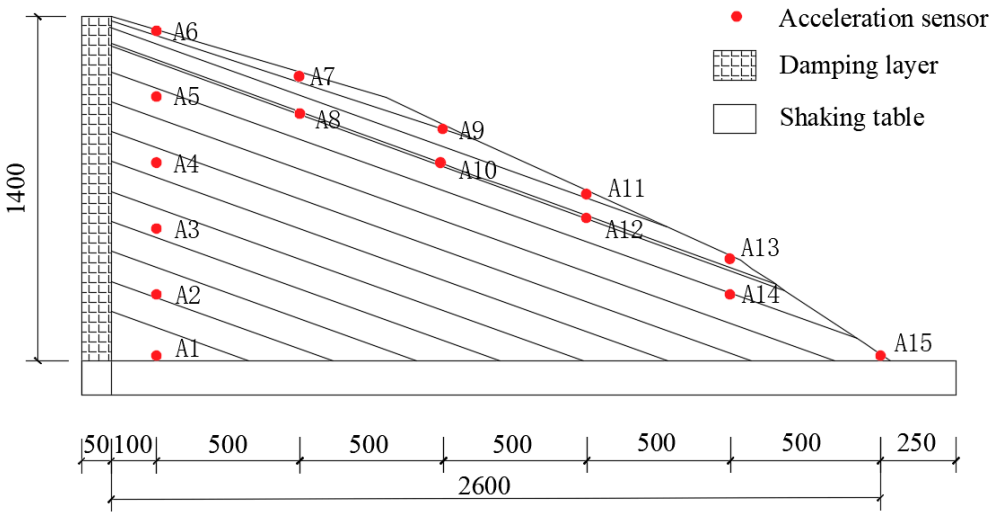

Figure 4. Layout position diagram of monitoring point A1–A15 (unit: mm).

2.5. Seismic Input and Loading Scheme

Structurally, the project area is located in the active tectonic area in northwest Yunnan. Neotectonic movement, deep tectonic deformation, fault activity, modern crustal deformation, etc. are relatively strong and are affected by seismic tectonic activities in the peripheral areas of the east and west sides. The basic seismic intensity in the project area is measured in degrees, and the peak horizontal acceleration is 0.30 g. As shown in Figure 5, the maximum acceleration of the input seismic wave was mainly concentrated within 6 s–10 s, and the peak acceleration occurred at 6.93 s. When considering inputting seismic waves with different peak accelerations, the seismic waves are proportionally scaled to preserve the consistent waveform of the seismic waves. The peak accelerations of horizontal and vertical seismic waves are scaled to 0.1 g, 0.2 g, 0.3 g, and 0.4 g.

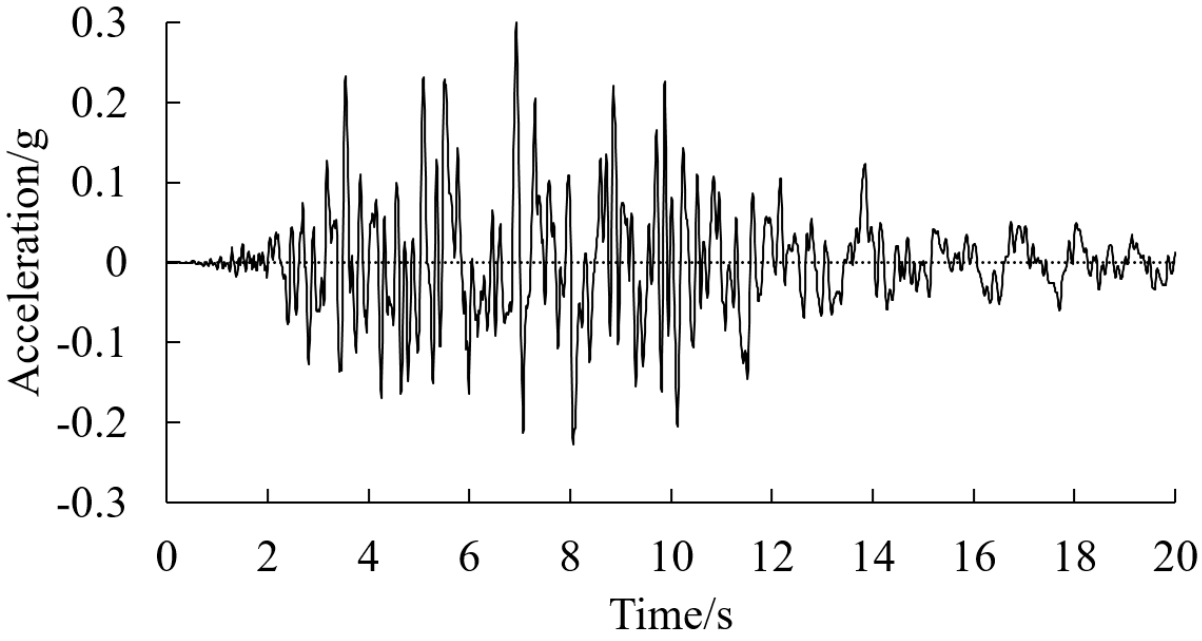

Figure 5. Input horizontal seismic wave curve.

The experimental simulation was divided into two conditions: no water and normal water level. First, the input of the seismic wave changed from a vertical seismic wave to a horizontal seismic wave, and the seismic acceleration gradually increased from 0 g to 0.4 g. Different seismic conditions were simulated.

In order to study the dynamic responses of slope models under different directions of seismic wave input conditions, the seismic load excitation direction was designed to be loaded first in the vertical direction and then in the horizontal direction, and the seismic acceleration was loaded in increments of 0.1 g, 0.2 g, 0.3 g, and 0.4 g. In order to study the influence of the mud deposition of reservoir water on the dynamic response of the model, a low water level test was conducted first, followed by a high water level test. The test plan is shown in Table 4, and the low water level condition is shown in Figure 6.

Table 4. Test loading conditions.

Loading Conditions	Earthquake Direction	Seismic Peak Acceleration/g	Reservoir Water Status
1	Vertical earthquake	0.1 g	Normal water level
2			No water level
3		0.2 g	Normal water level
4			No water level
5		0.3 g	Normal water level
6			No water level
7		0.4 g	Normal water level
8			No water level
9	Horizontal earthquake	0.1 g	Normal water level
10			No water level
11		0.2 g	Normal water level
12			No water level
13		0.3 g	Normal water level
14			No water level
15		0.4 g	Normal water level
16			No water level

Figure 6. Initial model.

3. Shaking Table Test Results and Analysis

3.1. Dynamic Response Analysis during Earthquake

By analyzing the data collected using the acceleration sensor in the slope model, we plotted the PGA change curve of each monitoring point in the model slope. Figure 7 shows the variation curve of the PGA amplification factor under the input vertical and horizontal earthquakes. H and N represent conditions with normal storage and no water, respectively. The analysis of Figure 7 shows the following:

1. It can be seen that when the input seismic acceleration was the same, the PGA at the normal water level was greater than that with no water, indicating that the mudding effect of reservoir water had a significant amplification effect on the PGA of the slope. The sedimentation of reservoir water also had a certain influence on the PGA distribution of the slope, and the enlarged area of PGA in the slope obviously increased after sedimentation. This is because after the front section of the weak interlayer was cemented, the cohesive force of the weak interlayer decreased, and the slope surface was damaged under the action of seismic waves, so the acceleration amplification effect at the slope angle was more obvious.
2. When both horizontal and vertical seismic waves were input, the acceleration response of the slope increased from the bottom to the top along the slope surface, reaching the maximum value at the top of the slope, with the maximum amplification factor of 2.5 with the input of vertical seismic waves, 3.25 with the input of horizontal seismic waves, and 0.83 times at the peak dynamic response of vertical seismic waves. By observing the slope of the folding line of the amplification coefficient change in PGA, it can be seen that, when increasing the slope height of the same height, the change in PGA at the slope angle of 250–500 mm is not significant. PGA rapidly increases in the middle part of the slope at 500–1000 mm, and the increase rate slows down again at 1000–1250 mm. Analyzing this phenomenon indicates that the impact of earthquakes on the slope is mainly evident in the middle part of the slope, and it can be considered that the middle part of the slope should be reinforced. It can reduce the PGA growth rate.
3. Upon comparing normal water storage conditions with no water level conditions, it can be observed that an increase in water level significantly increases the PGA amplification coefficient of the slope surface. When inputting vertical seismic waves, the peak value of PGA without water level is 1.82, and under normal water storage conditions, the peak value of PGA is 2.43, an increase of 33%. When inputting horizontal seismic waves, the PGA peak without water level is 2.76, and under normal water storage conditions, the PGA peak is 3.07, an increase of 11%. By analyzing the above data, it can be found that changes in water level have a significant impact on the dynamic response of the slope; especially, when inputting vertical seismic waves, the change in PGA is more severe. This indicates that, when analyzing the dynamic response of the slope, reservoir water and vertical earthquakes are two important factors affecting the stability of the slope.

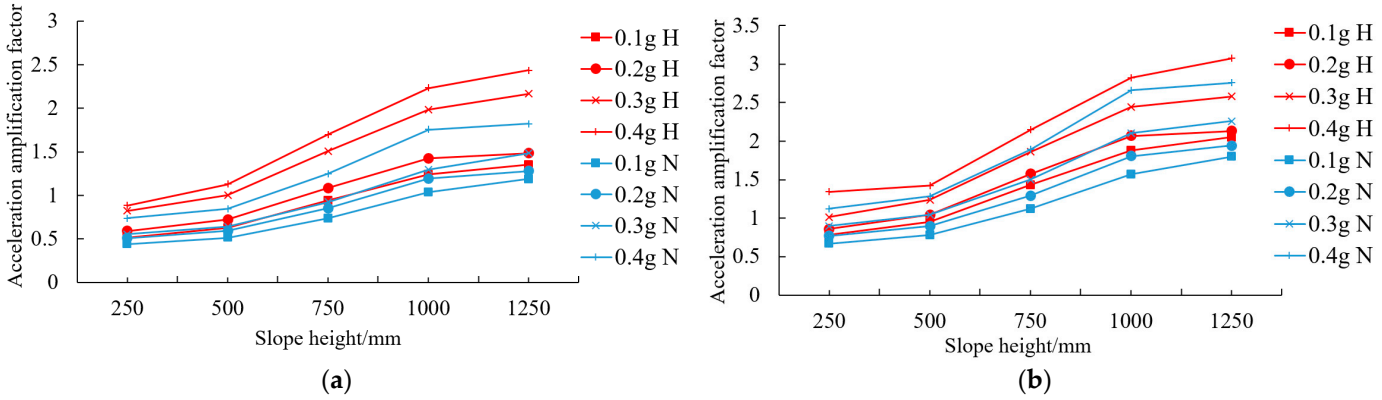

Figure 7. Variation curve of PGA amplification coefficient under different earthquakes. (**a**) Vertical seismic waves. (**b**) Horizontal seismic waves.

3.2. Analysis of Permanent Displacement during Earthquake

The maximum surface deformation of each measuring point under different seismic loads was plotted as a curve, from high to low, in different slope surface heights, and the relationship between the surface deformation of the slope and the input seismic acceleration was analyzed. Figure 8 shows the relationship between the maximum surface deformation and the input seismic acceleration. It can be seen from the diagram that the displacement of the slope surface increased with the increase in the input seismic wave acceleration.

For vertical input loads, when the input seismic acceleration was 0–0.3 g, the displacement increased uniformly. The surface displacement increased sharply when the input seismic acceleration reached 0.3 g. When the input seismic acceleration was 0.4 g, the maximum slope displacement appeared at up to 16.8 mm. When the input seismic acceleration reached 0.45 g, a steep drop in surface displacement occurred, which indicated that the dynamic response of a slope surface changes from the linear area to the plastic area.

For horizontal input loads, the displacement curve could be divided into three stages. In the first stage, when the input seismic acceleration was 0–0.3 g, the displacement increased uniformly, which was elastic deformation. In the second stage, when the input seismic acceleration was 0.3–0.45 g, the displacement first decreased and then increased, which was plastic deformation. The maximum slope displacement also appeared at up to 31.2 mm. In the third stage, when the input seismic acceleration reached 0.45 g, the surface displacement decreased abruptly, which was sliding destabilization, indicating that the landslide began at this time, and the slope was already unstable. When the input seismic acceleration reached 0.4 g, it coincided with the failure process of the slope in the test. The surface displacement increased sharply at first and then decreased sharply, indicating that the slope was unstable and slid completely, entering the post-failure stage. Upon comparing the data obtained from displacement measurement points arranged at different heights along the slope, it can be found that there is a sudden change in displacement at a distance of 400 mm from the top of the slope. The measurement points are located on the steeply inclined structural surface of the trailing edge, and obvious through cracks appear during the failure process.

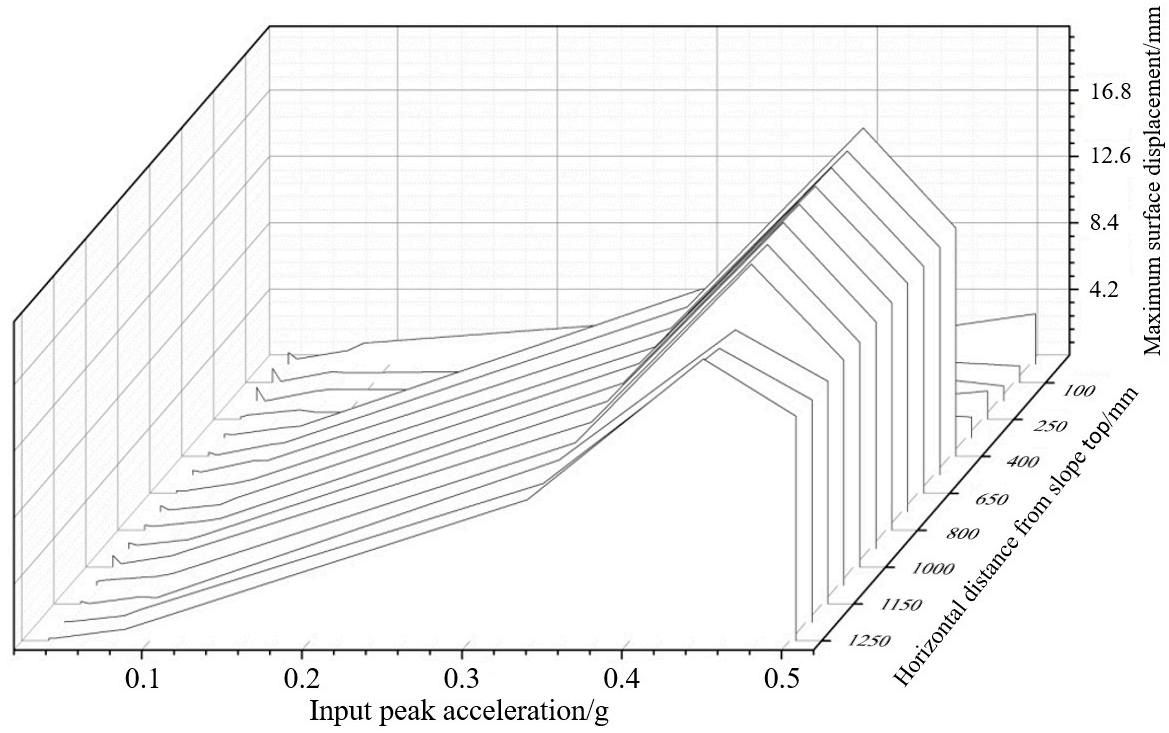

(**a**)

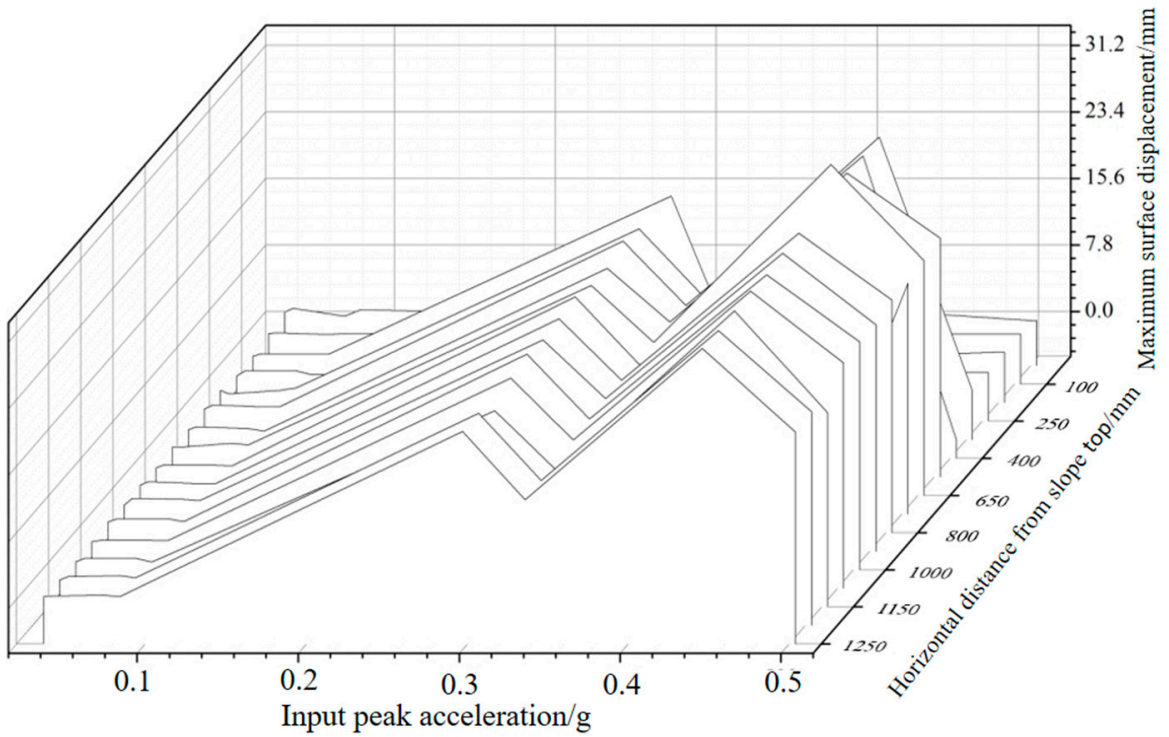

(**b**)

Figure 8. Evolution curve of surface displacement. (**a**) Vertical square load. (**b**) Horizontal load.

4. Numerical Simulation Analysis

4.1. Analysis Software and Constitutive Model Selection

Geostudio is a finite element software widely used in the field of geological engineering, in which the QUAKE/W modules and SLOPE/W modules are used to analyze dynamic responses and permanent displacements under the action of earthquakes. Therefore, in this paper, Geostudio software was used to calculate and analyze the dynamic response and permanent displacement of the slope under different seismic actions, in which the material constitutive model was the Linear Elastic Model. The Linear Elastic Model is immensely useful for education, testing, and verification purposes [26,27]. As there are no convergence problems with this model, many other issues can be resolved without convergence complications. For example, performing linear elastic analyses can be useful to determine the effects of various boundary conditions and confirm that they are being applied and used correctly or to confirm the effects of varying in situ conditions. The Linear Elastic Model in QUAKE/W is useful for verifying that the software provides the same solution.

4.2. The Establishment and Calculation of Numerical Model

The numerical model was established according to the optimal boundary requirements of the model proposed by Zhang Jiangwei et al. [28]. In the analysis of the model, the finite element mesh was divided into quadrilateral and triangular mesh, and the mesh size was determined according to the principle of 1/8–1/10 of the wavelength corresponding to the highest frequency of the input seismic wave, meaning the mesh needed to meet the accuracy requirements. The static boundary conditions of the finite element model were set as the left and right boundary normal constraint, the bottom fixed constraint, and the free slope. It should be noted that the above left and right boundary conditions should be changed to free states in the follow-up dynamic analysis. The model grouping and grid division are shown in Figure 9, and the finite element calculation model with an extended boundary at both ends considering the boundary effect is shown in Figure 10. Considering the influence of the tuff interlayer on the dynamic response of the slope, four columns of monitoring points were arranged on the slope surface, interlayer, overlying layer, and bedrock (as shown in Figure 11) to monitor the time-history variation process of acceleration, velocity, and displacement during an earthquake.

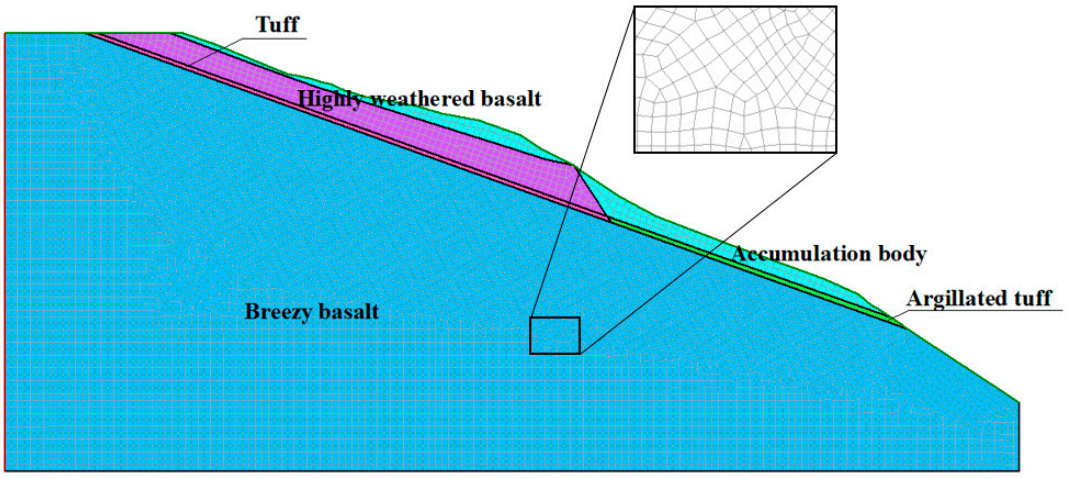

Figure 9. Model grouping and mesh division.

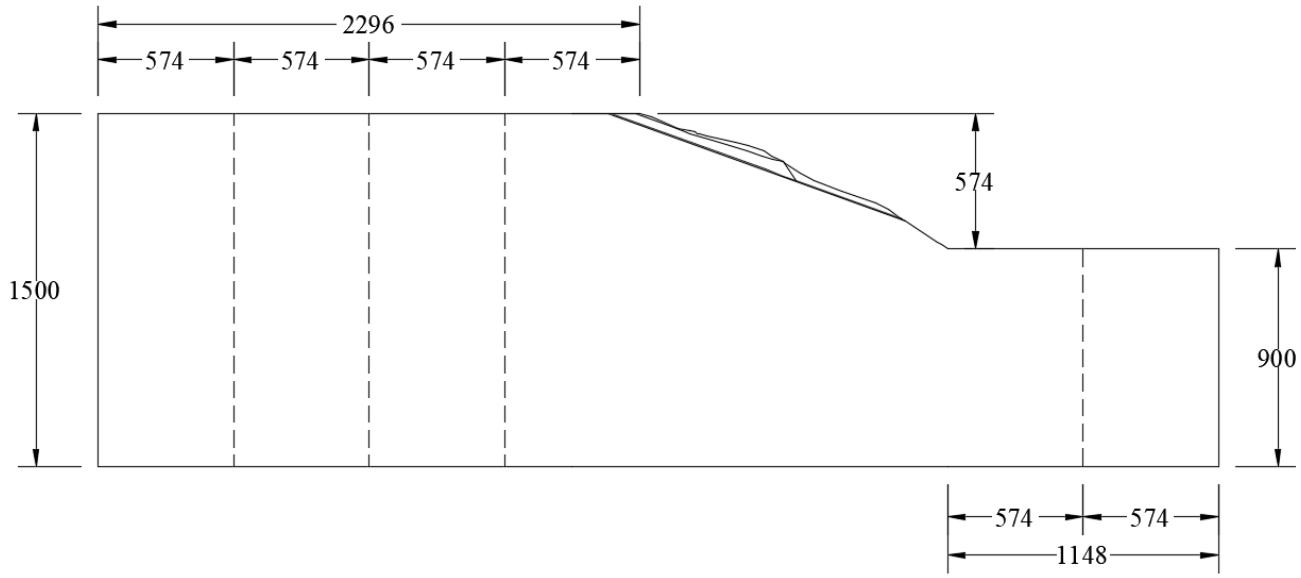

Figure 10. Finite element model of the slope (unit: m).

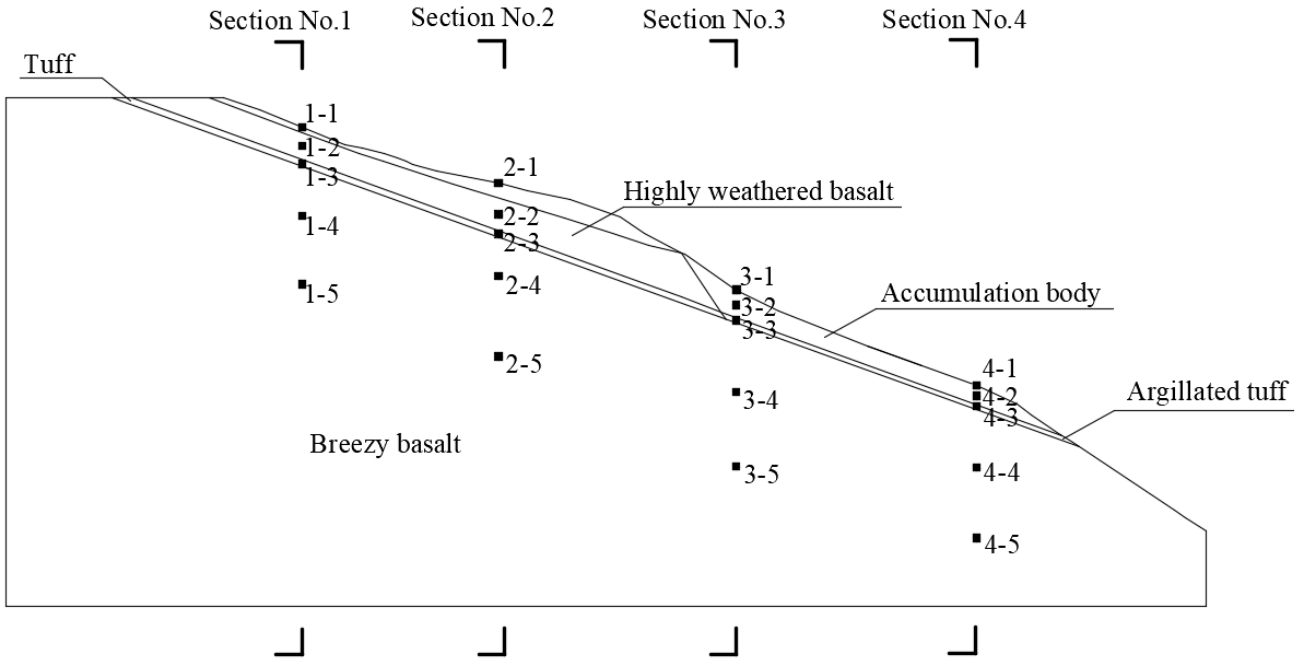

Figure 11. Layout of monitoring points.

4.3. Effect of Reservoir Water and Earthquake on Weak Sandwich Slope

4.3.1. Acceleration Response Analysis

In order to analyze the dynamic response of a slope to a vertical earthquake, the peak acceleration of the monitoring points on the slope surface was compared by inputting different vertical seismic accelerations. We defined the ratio of peak response acceleration at the monitoring point to peak input seismic wave acceleration as the acceleration amplification factor (PGA) at the monitoring point. Figure 12 shows the change in the peak acceleration of the slope, which is visually displayed by X-direction and Y-direction acceleration clouds during different earthquakes. It can be seen from the graph that with the increase in input seismic acceleration, the maximum area of peak acceleration was mainly distributed in the upper part of the slope, and the acceleration of rock mass near the slope surface was significantly different. The peak acceleration increased compared

with the peak input seismic wave. As the input vertical earthquake increased, the peak acceleration of the entire slope in the X direction gradually moved towards the foot of the slope. The peak acceleration of the whole slope in the Y direction increased significantly at the top and foot of the slope. The acceleration in the Y direction of the lower rock mass of the weak interlayer tended to increase in the slope, which indicated that the lower part of a slope is liable to be damaged when a vertical earthquake is involved.

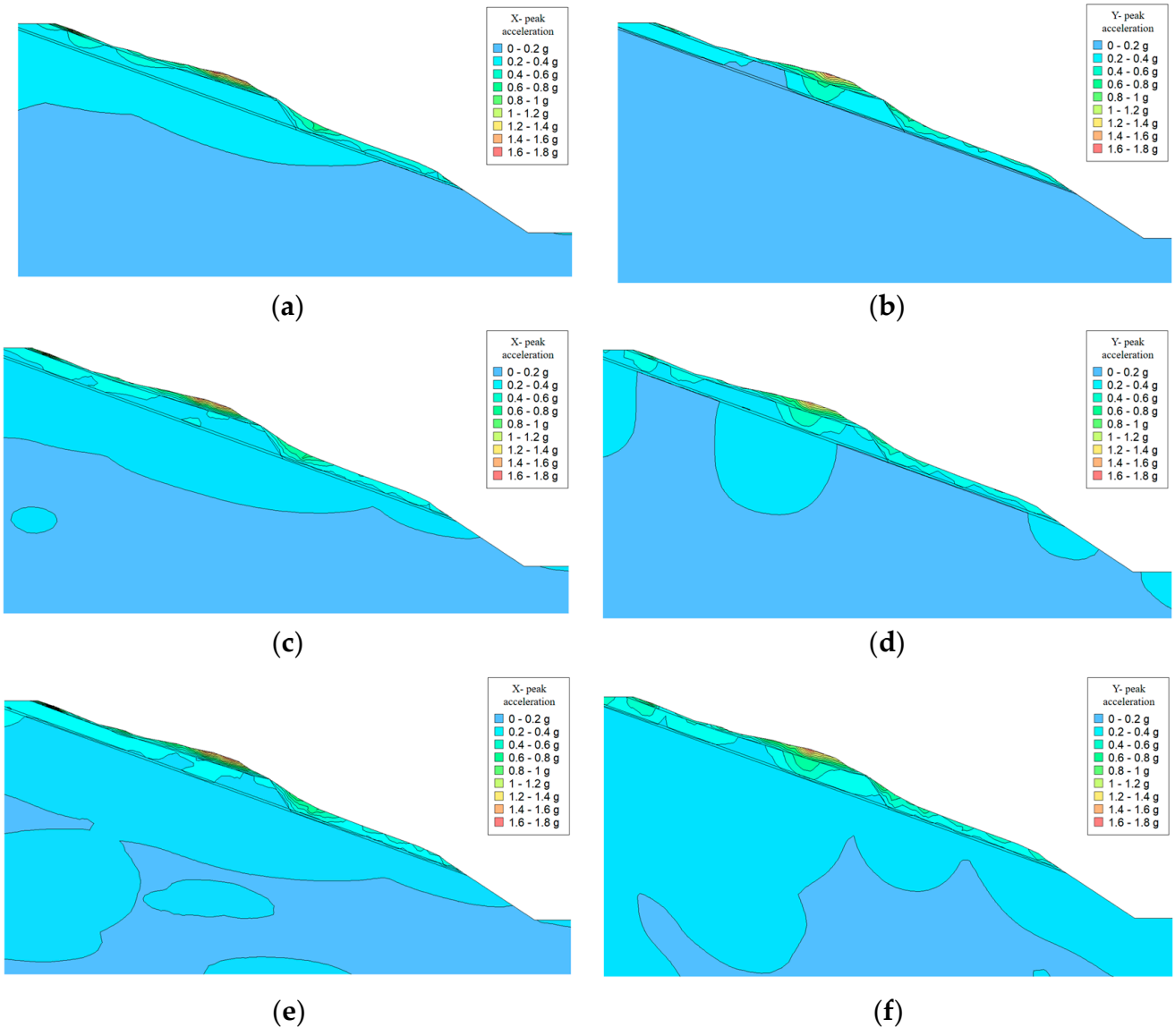

Figure 12. Acceleration cloud map in X and Y directions under different earthquakes. (**a**) X−direction acceleration cloud image at 0.1 g. (**b**) Y−direction acceleration cloud image at 0.1 g. (**c**) X−direction acceleration cloud image at 0.2 g. (**d**) Y−direction acceleration cloud image at 0.2 g. (**e**) X−direction acceleration cloud image at 0.3 g. (**f**) Y−direction acceleration cloud image at 0.3 g.

Compared with the acceleration cloud in the X and Y directions under the same seismic acceleration, with an increase in the input seismic wave, the acceleration response of the upper and lower rock mass of the weak interlayer gradually increases, but there is no obvious change in the dynamic response of the weak interlayer, which indicates that the weak interlayer has a certain energy absorption effect on the slope. However, when the input seismic wave acceleration is 0.3 g, the dynamic response of the upper and lower rock mass of the weak interlayer increases sharply. This indicates that the ability of the weak interlayer to absorb a seismic wave is saturated, and the

wave begins to affect the surrounding rock mass. Let us observe the acceleration cloud in the Y direction. With an increase in the input seismic wave, the dynamic response in the Y direction at the foot of slope is significantly larger than that in the X direction. This shows that the participation of vertical earthquakes has a strong influence on the dynamic response of the slope, which makes it easier for the slope to be destroyed at its foot.

In order to analyze the influence of mud in the front section of the tuff interlayer on the slope response, different vertical seismic accelerations were input to carry out slope dynamic response calculations. The analysis of Figure 13a,b is an intuitive means of determining whether the different heights of the slope surface are affected by the mudding of the weak interlayer. Upon comparing the PGA curve in the X and Y directions, the following conclusions were obtained:

1. By analyzing the PGA variation curves of different vertical seismic actions in the X direction, it can be seen from Figure 13a that the influence of reservoir water mud was mainly 300 m away from the bottom of the slope. With the increase in the input vertical seismic acceleration, the PGA within 300 m of the bottom of the slope changed most obviously among the four monitoring points on the slope surface. Compared with the normal water level and no water, only the PGA gap within 300 m of the bottom of the slope was large, and the PGA in other areas was very similar. This shows that when the weak interlayer in the front of a slope is muddled, the dynamic response of the slope will increase, i.e., the muddied, weak interlayer in the X direction can amplify the seismic wave.
2. By analyzing the PGA variation curves of different vertical seismic actions in the Y direction, it can be seen from Figure 13b that the influence of reservoir water mud was mainly 400 m from the bottom of the slope, and the PGA in other areas were very similar with the normal water level and with no water, which indicates that vertical seismic waves mainly affect the middle of a slope. When the weak interlayer in front of the slope was muddy, the dynamic response in the Y direction was mainly reflected in the middle and upper part of the slope. The maximum PGA value in the Y direction was 3.0, which could reach 0.85 times the maximum PGA value in the X direction, which was 3.5. These were very similar to the results of the model test, which showed that the numerical simulation had a high level of reliability.

By summarizing and analyzing the results in Figures 12 and 13, it is demonstrated that the presence of weak interlayers can cause seismic waves to overlap between the weak interlayers and the slope surface. The weak interlayers have the function of absorbing and isolating seismic waves, but their ability to absorb seismic waves is limited. When the seismic waves are large, the weak interlayers will stop absorbing seismic waves, thus exhibiting the phenomenon of amplifying seismic waves. When the weak interlayer undergoes mudification, the ability of the weak interlayer to absorb seismic waves decreases again, manifested as a significant increase in the transmission of seismic waves to the upper soil layer when they pass through the muddied weak interlayer; However, the muddy weak interlayer had little effect on other areas, which meant that the muddy weak interlayer was more likely to be destroyed in the project.

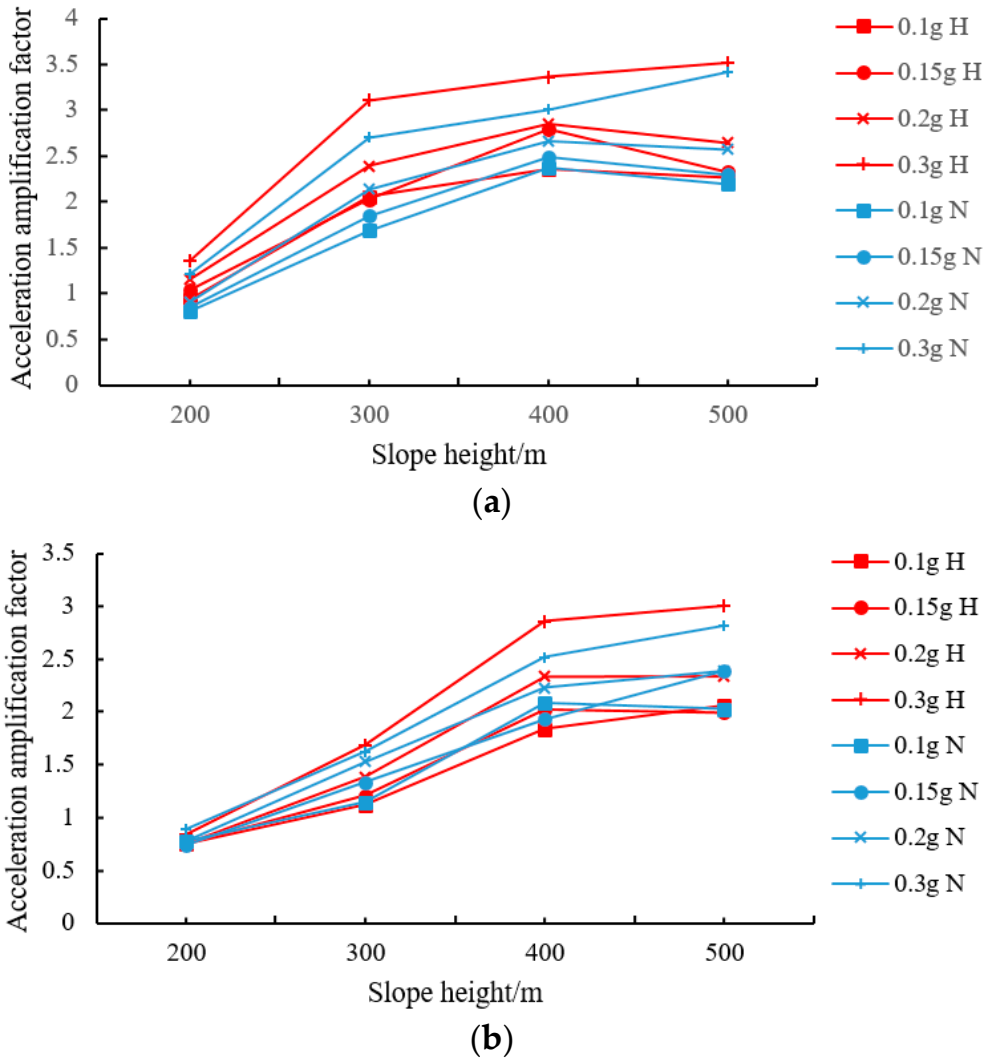

Figure 13. Variation curve of PGA amplification coefficient during different earthquakes. (**a**) Variation regularity of PGA during different vertical earthquakes in X direction. (**b**) Variation regularity of PGA during different vertical earthquakes in Y direction.

4.3.2. Permanent Displacement Analysis

In order to illustrate the influence of mud in the front section of tuff on permanent displacement, here, we considered the mud state in the front section of the interlayer. The calculation results are shown in Figure 14. It can be seen that the permanent displacement of the slope increased with the increase in the vertical seismic acceleration. Taking the slope displacement of the muddy interlayer as an example, the permanent displacement of the slope was 32 cm when the vertical earthquake reached 0.3 g. In the shaking table model test, when the input seismic wave reached 0.3 g, the measured displacement value was 0.86 mm, and the model similarity ratio was 400. The calculated true displacement value of the slope was 31.2 cm. The test results agreed with the numerical simulation results, which showed that the numerical simulation analysis method was feasible and had greater reliability.

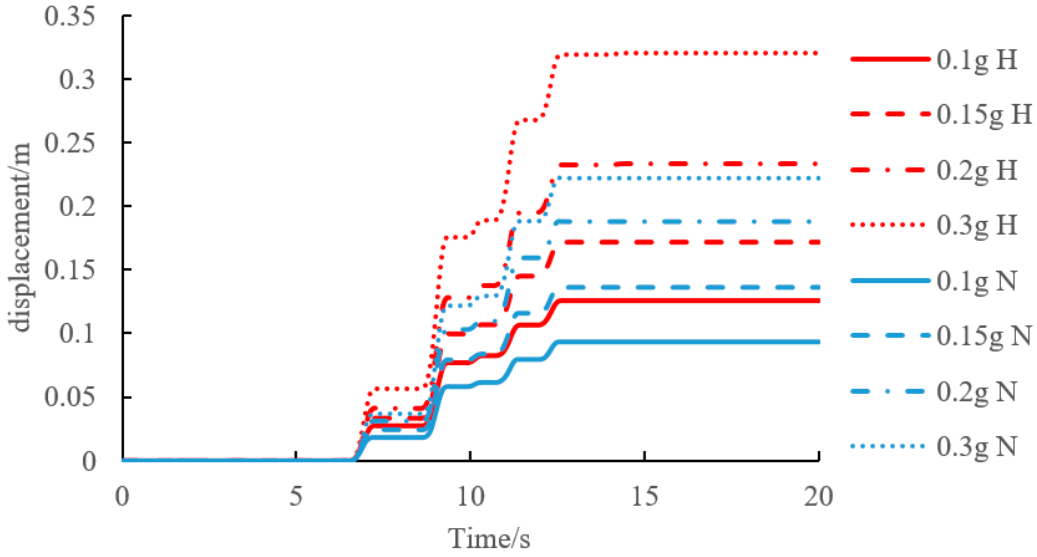

Figure 14. Permanent displacement of slope due to different seismic accelerations.

According to Jibson et al., when the permanent displacement of the slope exceeds 15 cm, the degree of failure of the slope is superelevation. It can be seen from the above figure that, if the argillization of reservoir water on the tuff interlayer and vertical seismic action are not considered, from the permanent displacement of the slope, the damage degree of the slope is only high, but there is argillization of reservoir water on the tuff interlayer in the project, so the actual damage caused to the slope is ultra-high.

5. Failure Pattern and Instability Mechanism Analysis

5.1. Slope Failure Pattern

After each input of different seismic waves, the crack positions and shedding parts of the slope surface after different seismic waves were determined by measuring the crack data on the model surface (see Figure 15). With the increase in the input seismic wave, the deformation and failure of model slope was a process of progressive evolution.

It can be seen from Figure 15a,b that when the input seismic acceleration was 0–0.1 g, no cracks occurred on the surface of the model slope after applying small seismic loads, i.e., the model slope vibration, which basically indicated that the model had not been damaged. When the input seismic acceleration was 0.2 g, a small number of cracks formed on the surface of the model slope, and a low level of shedding occurred in the middle and at the foot of the slope. It can be seen from Figure 15c,d that with the increase in the applied seismic load, i.e., when the input seismic acceleration was 0.3 g, the cracks on the surface of the model slope extended in the left and right directions, and there were penetrating cracks in the middle of the slope. The shedding phenomenon of the surface rock mass was mainly concentrated in the middle and lower part of the slope. It can be seen from Figure 15e,f that with the increase in the applied seismic load, when the input seismic acceleration was 0.4 g, several penetrating cracks appeared on the model slope. On the whole model surface, the slope surface was divided into several blocks, and the front section of the model with a weak interlayer (about 35 cm from the foot elevation) was completely destroyed.

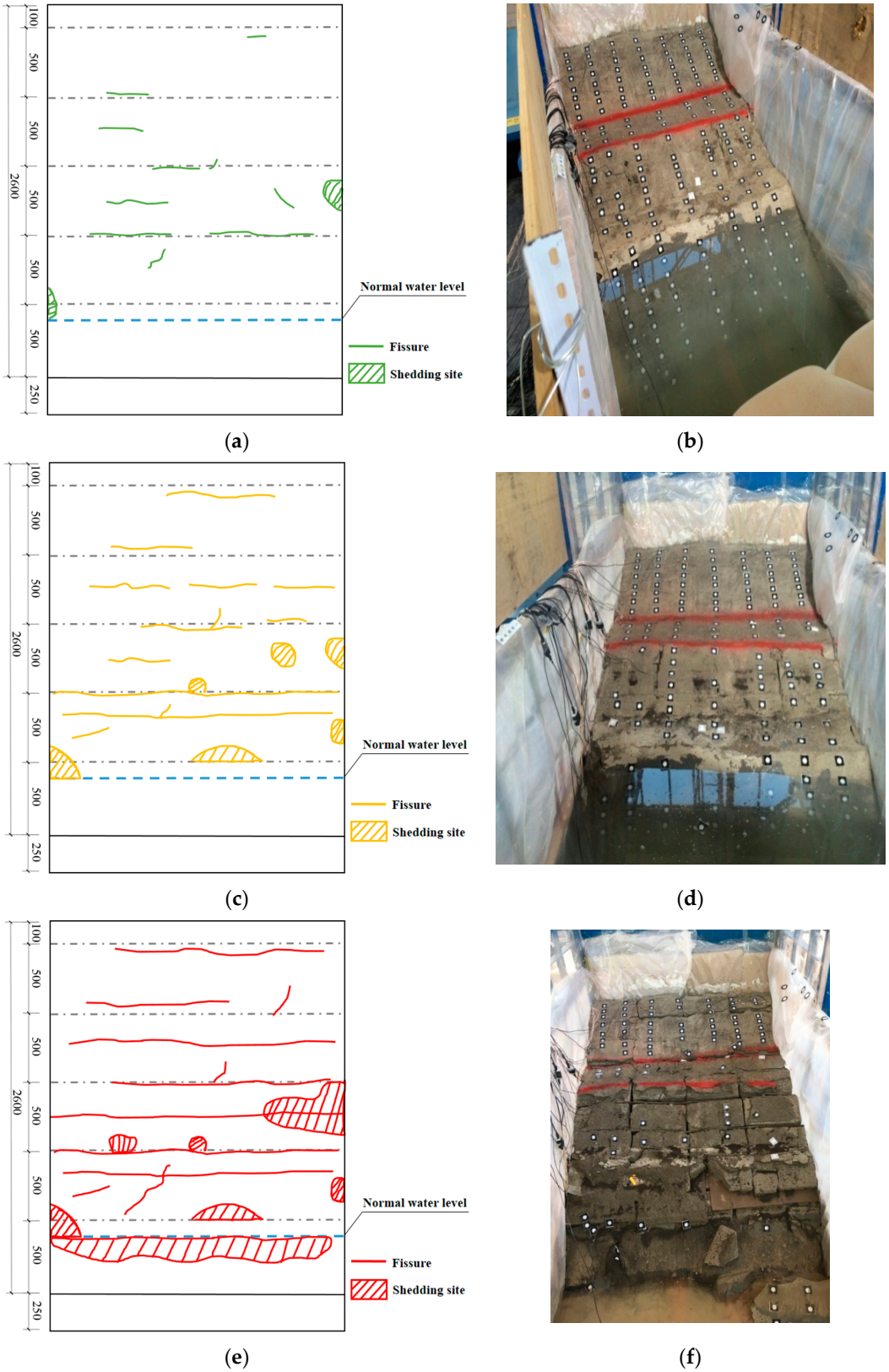

Figure 15. Failure of model slope during earthquake. (**a**) Description of 0–0.2 g crack. (**b**) A 0–0.2 g normal water level crack. (**c**) Description of 0.3 g crack. (**d**) Photograph of 0.3 g normal water level crack. (**e**) Depiction of 0.4 g cracks and damage. (**f**) Pictures depicting 0.4 cracks and damage.

When the model was unstable as a whole, there were a lot of cracks on the surface of the model. The damage was obvious with the change in model gradient, and the damage occurred completely at the foot of the slope. At a level of elevation of about 35 cm from the slope, the surface slope body overturned and slid out in block form. The reservoir water was pumped out, and the slope model was removed in layers, as shown in Figure 16.

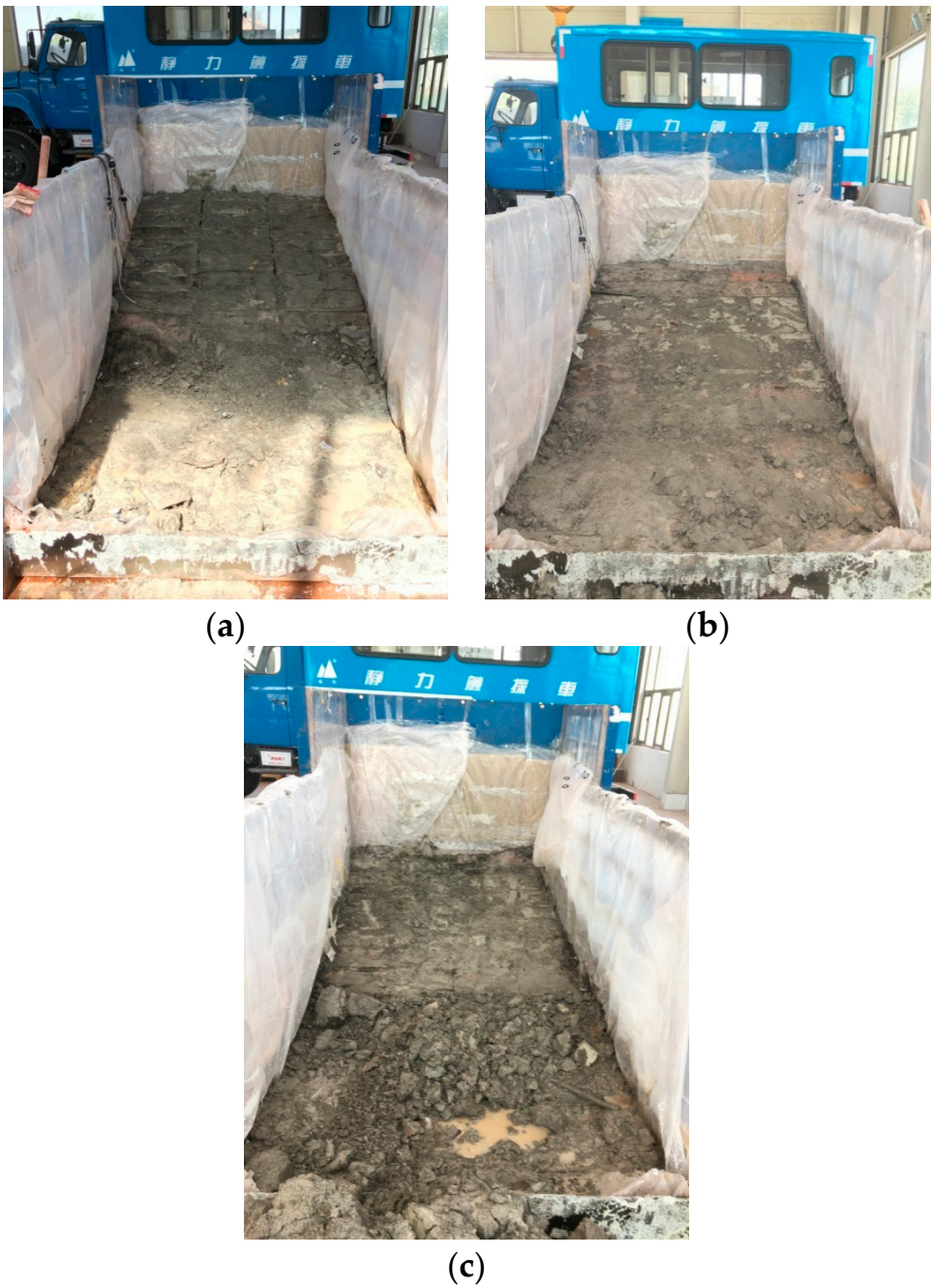

Figure 16. Photos of model layer removal. (**a**) Photo after removal of the first layer. (**b**) Photo after removal of the second layer. (**c**) Photo after removal of the third layer.

After the first layer was removed, the foot of the model slope was completely destroyed, the remaining slope body was relatively complete as a whole, and the surface water content of the remaining slope was high, which indicated that the surface slope body was destroyed and the reservoir water penetrated into the slope body. After removing the

second layer, the foot of the model slope was destroyed, the remaining slope was more complete as a whole, and the remaining slope surface was drier, showing that the reservoir water did not seep through the second layer of the slope surface. This showed that this layer of the slope surface did not undergo high levels of deformation and was relatively complete. It can be inferred that cracks appeared on the surface of the rear edge structure of the model, and the first layer was fully penetrated but did not extend to the second and third layers. After three layers were removed, the slope body was still dry, and the lowest layer of the model was seriously damaged near the foot of the slope, which was caused by damage to the foot due to reservoir water penetration. In conclusion, in the topmost slope of the model slope, overturning and sliding failure occurred to a great extent along the upper structural plane.

5.2. Induced Factors and Failure Mechanism of Slope Slip

Under the action of seismic load, due to the difference in the acceleration vector directions between the upper blocks of the slope and the phenomenon of the acceleration in the front block being greater than that in the rear block, cracks along joints occurred between blocks, which provided favorable conditions for block formation. The reservoir water seeped into the cracks and the upper structural plane, which quickly reached the saturation state, weakened its strength, further enlarged the cracks, and promoted the formation of massive and sliding zones. The sudden drop in the level of reservoir water caused a large increase in PGA on the uphill slope as well as a large increase in the downhill sliding force on the uphill slope. The acceleration in the rear block of the upper slope was greater than that in the front block, while the rear block pushed the front block to overturn and slide at a distance of 35 cm from the front edge to the bottom of the model, and they collided with each other during the sliding process to form debris flow based on the foot of the slope. Therefore, it can be concluded that the main process of a landslide is as follows: the upper part of the slope cracks due to an earthquake; with the increase in the intensity of the earthquake, the muddied weak interlayer in the front section of the slope forms a sliding surface; during an earthquake, sliding damage gradually occurs in the front section of the slope, and finally, accumulation occurs at the foot of the slope.

Through detailed analyses of acceleration, dynamic soil pressure, dynamic strain and displacement response during an earthquake, sliding induction factors, and failure mechanisms of model slopes, the slope failure phenomena we observed were analyzed. Cracks caused by seismic loads provide favorable conditions for the formation of induced landslides and the slide deformation of a slope body. Under the action of seismic load, different acceleration response directions exist among rock layers, which result in different rock layers in the direction of motion. Under the action of vertical seismic waves, upward vibrations between rock layers will occur, and speed and direction differences will occur during the deformation process of a slope during an earthquake, resulting in dislocation and tension between rock layers and the formation of cracks. Due to the difference in the acceleration response direction, under the action of horizontal seismic waves, the acceleration of the foot of a slope is higher than that of the top of a slope; thus, a tension crack is formed at the rock layer boundary.

6. Conclusions

In this study, using a shaking table test and finite element numerical simulation, the dynamic response law of slopes with weak interlayers under the combined action of reservoir water and seismic force was defined, and the ring breaking mechanism of weak interlayers was revealed. The main conclusions are as follows:

1. Seismic waves are affected by weak interlayers, which overlap repeatedly between a weak interlayer and a slope surface. The acceleration amplification effect is about 1.8 times larger than that of a homogeneous slope. The acceleration response of the input vertical and horizontal seismic waves in a slope is magnified from the bottom to the top along the slope surface and reaches the maximum value at the top of the slope. A vertical earthquake has a significant influence on the dynamic response of a slope. The magnification factor of peak acceleration can reach 0.83 times the horizontal peak acceleration. An increase in the intensity of a vertical earthquake is more likely to induce damage on the top and in the middle of a slope.
2. When considering the mud action of reservoir water on weak interlayers, with the increase in the input seismic acceleration, sliding failure first occurs in the mud area located in the weak interlayer. The shear entrance and shear exit of slope sliding are located in the middle and at the foot of the slope, respectively, which indicates that the stability of the weak interlayer directly affected by reservoir water is the worst.
3. The displacement of a slope can be generalized into three stages with the increase in a seismic wave. The first stage is elastic deformation, when the displacement increases uniformly from 0 to 0.3 g. In the second stage, when the displacement is 0.3–0.45 g, the displacement first decreases and then increases, which is the plastic deformation stage. The maximum displacement of the slope surface also appears, up to 31.2 mm. The third stage is when the surface displacement decreases sharply after reaching 0.45 g, which is the sliding destabilization stage, indicating that the slope begins to slide and destabilize at this time.
4. The failure mode of the slope is as follows: cracking occurs in the upper part of the slope due to an earthquake. With the increase in the intensity of the earthquake and reservoir water infiltration, the crack propagation is aggravated, and sliding damage occurs gradually in the front section of the slope. Finally, accumulation occurs at the foot of the slope. The failure mode of the slope model reveals that the sliding surface is controlled by a weak interlayer. When a strong earthquake and the water level in the reservoir area jointly affect the weak-interlayer slope, the slope is in the plastic deformation and instability stage. The stability of the slope may be overestimated, and sliding instability easily occurs. Therefore, monitoring and treatment must be carried out.

In the numerical simulation part of this study, we only considered the effect of the static water load of reservoir water, which is not in line with reality and requires the dynamic calculation of fluid structure coupling.

Author Contributions: Conceptualization, H.T. and W.N.; methodology, H.T. and W.N.; software, H.T. and W.N.; validation, H.T. and W.N.; formal analysis, H.T. and W.N.; investigation, H.T. and W.N.; resources, H.T. and W.N.; data curation, H.T. and W.N.; writing—original draft preparation, H.T. and W.N.; writing—review and editing, H.T. and W.N. All authors have read and agreed to the published version of the manuscript.

Funding: This research received no external funding.

Institutional Review Board Statement: Not applicable.

Informed Consent Statement: Not applicable.

Data Availability Statement: Data used to support the findings of this study are available from the corresponding author upon request.

Conflicts of Interest: The authors declare that the research was conducted in the absence of any commercial or financial relationships that could be construed as potential conflicts of interest.

References

1. Zhang, J.M. Research status and development trend of rock slope stability with weak interlayer. *Chin. J. Eng. Geol.* **2020**, *28*, 626–638. [CrossRef]
2. Niu, Y.; Yang, X.Z.; Zhao, J.L.; Ji, W.K. Seismic stability analysis of slope with sandwich based on upper limit analysis. *J. Highw. Transp. Sci. Technol.* **2019**, *36*, 38–45.
3. Lin, M.L.; Lin, C.H.; Li, C.H.; Liu, C.Y.; Hung, C.H. 3D modeling of the ground deformation along the fault rupture and its impact on engineering structures: Insights from the 1999 Chi-Chi earthquake, Shigang District, Taiwan. *Eng. Geol.* **2021**, *281*, 105993. [CrossRef]
4. Li, S.D.; Li, X.; Zhang, J.; He, J.M.; Li, S.H.; Wang, Y.C. Research on formation mechanism of Tangjiashan landslide and overall stability of barrier dam. *Chin. J. Rock Mech. Eng.* **2010**, *29* (Suppl. S1), 2908–2915.
5. Xu, L.; Pei, X.J.; Wu, J.H. Stability evaluation and treatment of Zhengjiashan Landslide in Sichuan Earthquake stricken area. *J. Chang. Inst. Technol. (Nat. Sci. Ed.)* **2010**, *11*, 68–70+81.
6. Haeri, S.M.; Kavand, A.; Rahmani, I.; Torabi, H. Response of a group of piles to liquefaction-induced lateral spreading by large scale shake table testing. *Soil Dyn. Earthq. Eng.* **2012**, *38*, 25–45. [CrossRef]
7. Panah, A.K.; Eftekhari, Z. Shaking table tests on polymeric-strip reinforced-soil walls adjacent to a rock slope. *Geotext. Geomembr.* **2021**, *49*, 737–756. [CrossRef]
8. Wang, H.L.; Jiang, Z.H.; Xu, W.Y.; Wang, R.B.; Xie, W.C. Physical model test on deformation and failure mechanism of deposit landslide under gradient rainfall. *Bull. Eng. Geol. Env.* **2022**, *81*, 66. [CrossRef]
9. Xiao, J.F.; Li, Y.A.; Hu, Y.; Zhang, S.; Cai, J.M. Model tests on deformation characteristics of ancient bank landslide under water level fluctuation and rainfall. *Rock Soil Mech.* **2021**, *42*, 471–480. [CrossRef]
10. Mburu, J.W.; Li, A.-J.; Lin, H.-D.; Lu, C.-W. Investigations of Unsaturated Slopes Subjected to Rainfall Infiltration Using Numerical Approaches—A Parametric Study and Comparative Review. *Sustainability* **2022**, *14*, 14465. [CrossRef]
11. Zhang, M.S.; Dong, Y.; Sun, P.P. Impact of reservoir impoundment-caused groundwater level changes on regional slope stability: A case study in the Loess Plateau of Western China. Environ. *Earth Sci.* **2012**, *66*, 1715–1725. [CrossRef]
12. Manenti, S.; Amicarelli, A.; Palazzolo, N.; Bordoni, M.; Creaco, E.; Meisina, C. Post-Failure Dynamics of Rainfall-Induced Landslide in Oltrepò Pavese. *Water* **2020**, *12*, 2555. [CrossRef]
13. Wang, R.; Wan, J.; Cheng, R.; Wang, Y.; Wang, Z. Physical and Numerical Simulation of the Mechanism Underpinning Accumulation Layer Deformation, Instability, and Movement Caused by Changing Reservoir Water Levels. *Water* **2023**, *15*, 1289. [CrossRef]
14. Jiang, Z.H.; Wang, H.L.; Xie, W.C. Deformation mechanism of deposit landslide induced by fluctuations of reservoir water level based on physical model tests. Environ. *Earth Sci.* **2021**, *80*, 410. [CrossRef]
15. Upomo, T.C.; Chang, M.; Kusumawardani, R.; Prayitno, G.A.; Kuo, C.-P.; Nugroho, U. Assessment of Petobo Flowslide Induced by Soil Liquefaction during 2018 Palu–Donggala Indonesian Earthquake. *Sustainability* **2023**, *15*, 5371. [CrossRef]
16. Kim, H.; Kim, D.; Lee, Y.; Kim, H. Effect of Soil Box Boundary Conditions on Dynamic Behavior of Model Soil in 1 g Shaking Table Test. *Appl. Sci.* **2020**, *10*, 4642. [CrossRef]
17. WANG, K.L.; LIN, M.L. Initiation and displacement of landslide induced by earthquake—A study of shaking table model slope test. *Eng. Geol.* **2011**, *122*, 106–114. [CrossRef]
18. Yang, H.; Cui, S.; Pei, X.; Fan, X.; Lei, J. Multiple earthquake-induced progressive failure of bedding slopes with a saturated weak layer: Shaking table model tests. *Soil Dyn. Earthq. Eng.* **2023**, *170*, 107906. [CrossRef]
19. Wang, L.W.; Wen, H.; Zhang, Z.P.; Du, Y.X.; Fu, X.D. Seismic dynamic response analysis and stability evaluation of Ganjiazhai Landslide based on QUAKE/W and SLOPE/W. *Sci. Technol. Eng.* **2018**, *18*, 274–280.
20. Yan, Z.X.; Gao, L.; Peng, N.B.; Ren, Z.H.; Guo, B. Study on seismic dynamic response of bedding rock slope. *Rock Soil Mech.* **2012**, *33* (Suppl. S2), 85–90. [CrossRef]
21. Jin, Y.; Kim, D.; Jeong, S.; Kim, H. Analysis of Multilayered Ground Amplification Characteristics by Scaled-Down Model Tests. *Appl. Sci.* **2022**, *12*, 3432. [CrossRef]
22. Huang, D.; Xie, Z.Z.; Song, Y.X.; Meng, Q.J.; Luo, S.L. Centrifuge model test study on the toppling deformation of the anti-dip soft-hard interbedded rock slopes. *Chin. J. Rock Mech. Eng.* **2021**, *40*, 1357–1368. [CrossRef]
23. Málaga-Chuquitaype, C. Estimation of peak displacements in steel structures through dimensional analysis and the efficiency of alternative ground-motion time and length scales. *Eng. Struct.* **2015**, *101*, 264–278. [CrossRef]
24. Guo, M.-Z.; Gu, K.-S.; Wang, C. Dynamic Response and Failure Process of a Counter-Bedding Rock Slope under Strong Earthquake Conditions. *Symmetry* **2022**, *14*, 103. [CrossRef]
25. Buckingham, E. On physically similar systems, illustrations of the use of dimensional equations. *Phys. Rev.* **1914**, *4*, 345–376. [CrossRef]
26. Cai, G.-Q.; Su, Y.-L.; Zhou, A.-N.; Yin, F.-J.; Shi, Y.-H. An elastic-viscoplastic model for time-dependent behavior of unsaturated soils. *Comput. Geotech. Vol.* **2023**, *159*, 105415. [CrossRef]

27. Rizzitano, S.; Cascone, E.; Biondi, G. Oupling of topographic and stratigraphic effects on seismic response of slopes through 2D linear and equivalent linear analyses. *Soil Dyn. Earthq. Eng.* **2014**, *67*, 66–84. [CrossRef]
28. Zhang, J.W.; Zhou, A.H.; Chi, M.J.; Wang, Y.S.; Chen, S. Study on optimal boundary range in numerical simulation of slope seismic response. *J. Disaster Prev. Mitig. Eng.* **2022**, *42*, 34–41. [CrossRef]